Journal of Alloys and Compounds 1076 (2026) 189327

Contents lists available at ScienceDirect

Journal of Alloys and Compounds

journal homepage: www.elsevier.com/locate/jalcom

Selective phase dissolution as a route to nanoporous titanium with tailored properties

N.T. Panagiotopoulos [a], L. Koutsokeras [b,c], A.M. Jorge Jr [d,e,f], G.I. Lampronti [a], K. Georgarakis [g], W.J. Botta [d], A.L. Greer [a,*]

[a] Department of Materials Science & Metallurgy, University of Cambridge, Cambridge CB3 0FS, UK
[b] Department of Physics, National and Kapodistrian University of Athens, Athens 15784, Greece
[c] Cyprus University of Technology, Department of Mechanical Engineering and Materials Science and Engineering, Cyprus
[d] Federal University of São Carlos, DEMa, São Carlos, SP 13565-905, Brazil
[e] Univ. Grenoble Alpes, Univ. Savoie Mont Blanc, CNRS, Grenoble INP (Institute of engineering, Univ. Grenoble Alpes), LEPMI, Grenoble 38000, France
[f] Univ. Grenoble Alpes, CNRS, Grenoble INP, SIMaP, Grenoble38000, France
[g] School of Aerospace, Transport and Manufacturing, Cranfield University, Cranfield MK43 0AL, UK

ARTICLE INFO

Keywords:
Cellular precipitation
Nanoporous titanium
Reflectivity
Selective phase dissolution
Wettability

ABSTRACT

Selective dissolution of one phase from as-cast two-phase alloy microstructures is explored as a route to nanoporous solids with high specific-surface-area (SSA) competitive with the values attainable by established dealloying methods. The chosen alloy system, Ti-Sc, is studied over a composition range from $Ti_{75}Sc_{25}$ to $Ti_{25}Sc_{75}$ (at %). In as-cast alloys, the phase constitution is characterized, and the mechanism of microstructural development is elucidated. The Sc-rich phase can be selectively dissolved from the as-cast alloys, yielding nanoporous Ti samples. The SSA, wettability and optical reflectivity of the nanoporous samples are characterized. Selection of as-cast composition permits control of these properties. It is concluded that selective dissolution from two-phase microstructures is a viable route to useful nanoporous solids. Results from different casting conditions, and from subsequent solid-state heat treatment, indicate paths to optimization of the nanoporous morphology and to higher SSA.

1. Introduction

In recent decades, there has been growing interest in nanoporous materials, characterized by high specific-surface-area (SSA). Nanoporous metals (including Au, Pt, Pd, Cu, Ni, and Ti-based alloys) have many applications, including in light harvesting [1–3], surface-enhanced Raman spectroscopy (SERS) [4] important for molecular detection, photo- and electrochemical catalysis and sensing [5,6], and energy conversion and storage [7–9] such as in batteries and fuel-cells.

Nanoporous metals have mostly been made by dealloying, i.e. selective dissolution of one or more alloying elements from a single-phase alloy. Using chemical or electrochemical dissolution, across a wide range of alloys, similar nanoporous microstructures are produced via the mechanisms elucidated by Erlebacher et al. [10]. While the electrochemical method is the most widely studied, dealloying is also possible with other external media: liquid metal, solid metal, and vapor phase. The capabilities of these methods have been extensively reviewed [11,12]: control over alloy composition, dealloying route, and post-dealloying treatments enables tailored morphologies — from two-dimensional membranes and thin films to three-dimensional bulk monoliths. Furthermore, the ability to engineer hierarchical porosity, from micropores to macropores within a single structure, has unlocked new opportunities in electrocatalysis, sensing, energy storage, and biomedical implants, suggesting morphology-controlled dealloying as a scalable and increasingly indispensable fabrication strategy for next-generation functional materials [13].

It is intrinsic in all the dealloying methods that the development of the nanoporous microstructure is concurrent with the selective dissolution. Despite the control now demonstrated over the scale and morphology of the nanoporosity, it is of interest to explore whether the degree or nature of such control could be extended by separating the

* Corresponding author.
E-mail addresses: np488@cam.ac.uk (N.T. Panagiotopoulos), lkoutsok@phys.uoa.gr (L. Koutsokeras), moreira@ufscar.br (A.M. Jorge), gil21@cam.ac.uk (G.I. Lampronti), k.georgarakis@cranfield.ac.uk (K. Georgarakis), wjbotta@ufscar.br (W.J. Botta), alg13@cam.ac.uk (A.L. Greer).

https://doi.org/10.1016/j.jallcom.2026.189327
Received 26 April 2026; Received in revised form 7 June 2026; Accepted 18 June 2026
Available online 22 June 2026
0925-8388/© 2026 The Author(s). Published by Elsevier B.V. This is an open access article under the CC BY license (http://creativecommons.org/licenses/by/4.0/).

dissolution and the microstructure development.

The possibility of such a separation was demonstrated by some of the present authors for the alloy system Ti-Sc [14]. Cast alloys showed a fine-scale (sub-μm) two-phase microstructure, attributed to a solid-state decomposition after initial solidification. It was further shown that one of the phases could be selectively dissolved, the residual solid being nanoporous and Ti-rich. Building on these results, we take Ti-Sc as a model system for further study. There has been some direct interest in Ti-Sc composites [15], but our focus is on how selective phase dissolution can be applied to obtain a nanoporous solid. Nanoporous titanium and titanium alloys have many potential uses, notably for biomedical applications [16].

Setting aside potential applications of a particular system, our main objectives in the present work are to: (i) understand better the solid-state transformation that gives such a usefully fine microstructure; (ii) explore the prospects for control of the alloy microstructure, and thereby tailoring of the extent and characteristic length-scale of the porosity that can be achieved. This exploration includes: characterizing a wider range of compositions than in [14]; and study of the effects of differing solidification conditions and of subsequent solid-state annealing. For the nanoporous samples resulting from selective dissolution, we characterize the associated properties: effective surface area, wettability, optical reflectivity.

We note that in producing porous metals, selective dissolution from a two-phase microstructure has been applied in several other alloys, for example for Zn-Sn-(Bi) [17,18] and Cu-Ag-Al [19] alloys for battery electrodes. In these cases, however, the two-phase microstructures were generated by eutectic solidification; such microstructures are inevitably coarser than those arising from solid-state decomposition.

2. Experimental methods

The alloys were produced by arc-melting together titanium (99.98% purity, Alfa Aesar) and scandium (99.9% purity, Sendai Wako Pure Chemicals Ltd). Before casting, the arc-melting chamber was evacuated to a base pressure of 5×10^{-6} mbar, then backfilled with argon to 500 mbar in which pure titanium was melted as getter for residual oxygen. Arc-melted 'bulk-cast' ingots, ~12 mm in diameter, were formed on the water-cooled copper hearth; these were re-melted at least five times to ensure compositional uniformity. Portions of the bulk-cast ingots were melted and 'suction-cast' as rods, 5 mm long and 2 mm in diameter, in a copper mold.

As noted in §3.1, the samples consist of two phases, one Ti-rich, the other Sc-rich. Some of the samples were sealed in fused-silica tubes under vacuum and subjected to isochronal (4 h) anneals in a radiation furnace, then rapidly quenched by fracturing the tubes upon immersion in a water bath.

Slices ~1 mm thick were cut from the cast samples, mechanically ground, and mirror-polished using 0.25 μm diamond paste. The samples were then cleaned sequentially in acetone and ethanol in an ultrasonic bath, followed by immersion in 70% HNO_3 for 20 h, at room temperature, to ensure complete dissolution of the Sc-rich phase to the extent accessible by EDS and conventional XRD measurements [14]. The Ti-rich phase appears resistant to acid attack, while the Sc-rich phase dissolves. Following this selective dissolution, the nanoporous Ti samples (porosity >50%) occasionally exhibited spontaneous ignition upon exposure to air. This is attributed to rapid exothermic oxidation of the high surface area structure. To mitigate this, samples were immediately transferred to five or more sequential deionized water baths (a few seconds each) and rinsed under running deionized water prior to drying. This promotes controlled formation of a passivating TiO_2 layer while dissipating heat, effectively suppressing ignition.

The phase constitution of the as-cast and chemically treated alloys was analyzed using X-ray diffraction (XRD) (PANalytical X'Pert PRO MPD, CuKα radiation, with a Si NIST standard to refine the instrument's resolution function). Rietveld analysis (TOPAS Academic V7 software [20]) quantified the volume fractions of the phases to an accuracy of ±1–2%; the estimated standard deviation relates to the stability of the mathematical fitting [21]. The X-ray background was modeled using a seven-parameter Chebyshev function. The Bragg peaks were fitted by combining Lorentzian and Gaussian functions representing the contributions (presumed isotropic in each case) to peak width, respectively, from limited grain size and from inhomogeneous strain. An 8th-order spherical-harmonics model was used to describe the preferred orientation of the two phases.

The compositions of the as-cast Ti-Sc alloys were determined using X-ray energy-dispersive spectroscopy at an acceleration voltage of 15 keV (Hitachi TM4000Plus, with Oxford Instruments EDS). The microstructure of the NP-Ti samples was examined using extremely high-resolution scanning electron microscopy (XHR-SEM) (FEI Magellan 400 XHR SEM with field emission (FEG) source, operating at 3 keV with in-lens detectors), as well as a high-resolution (HR) FEG-SEM (Zeiss Ultra−55) operated at 10 keV. The latter, equipped with a Bruker AXS EDS system, also was used for chemical composition analysis of the NP-Ti samples. Micrographs of annealed samples were acquired in a HR FEG-SEM (JEOL JSM-7800F) operated at 15 keV.

The hardness of the as-cast and annealed samples was measured using a Vickers microhardness tester under loads from 200 g to 1 kg. For each sample, a minimum of 14 and a maximum of 30 indentations were performed, and the measured hardness showed no significant variation with applied load.

The specific-surface-area of NP-Ti samples, leached for one week to ensure full selective dissolution, was determined using the Brunauer-Emmett-Teller (BET) method. The required nitrogen adsorption isotherms were obtained using a Micrometrics ASAP 2020 surface-area analyzer. The fitting range was selected according to standard BET criteria, ensuring linearity of the BET plot and physically meaningful values of the BET constant. Preliminary measurements of the contact angle of deionized water (droplets of ~6 μL) on the surface of NP-Ti were made using a custom-built setup analyzing photographs (acquired with a Nikon COOLPIX S51 within seconds to minutes) with ImageJ software. Measurements of this kind can provide valuable insights into surface properties [22].

Light reflection from the sample surfaces was characterized using specular and diffusive reflectometry (ThetaMetrisis FR-Basic system). An integrated-reflectance sphere and the spectral width of the UV-Vis light source allowed for precise measurement of the reflected light.

3. Results and discussion

3.1. Phase constitution

X-ray diffraction shows that the bulk-cast Ti-Sc alloys consist of two phases (Fig. 1). As expected from the equilibrium diagram [23] (Suppl. Mater. Fig. S1), these are the hexagonal-close-packed terminal solid solutions α-Ti(Sc) and α-Sc(Ti) Fig. S2). For each phase, its lattice parameters are the same in all samples and are intermediate between those of the pure elements, indicating some solid solubility in both (Table S2). Figure S3 shows the lattice parameters interpreted according to Vegard's law. On a linear interpolation between the lattice parameters of the elements, the terminal solid solutions are estimated to have the compositions (at%) $Ti_{91}Sc_9$ and Ti_8Sc_{92}. After selective dissolution, the samples contain only the α-Ti(Sc) phase (Fig. S4), and EDS analysis of this gives the composition as ~8 at% Sc, in reasonable agreement with the estimate from Vegard's law.

The volume fractions of the two phases in each cast alloy can be estimated from the phase compositions already determined, by applying the lever rule for each sample composition to obtain the atomic fraction of each phase, and then compensating for the different volumes per atom (§S4). These estimated volume fractions (Fig. 2) are reasonably confirmed by Rietveld refinement of the X-ray pattern. This refinement, however, takes the two phases to be elemental (i.e. pure α-Ti and pure

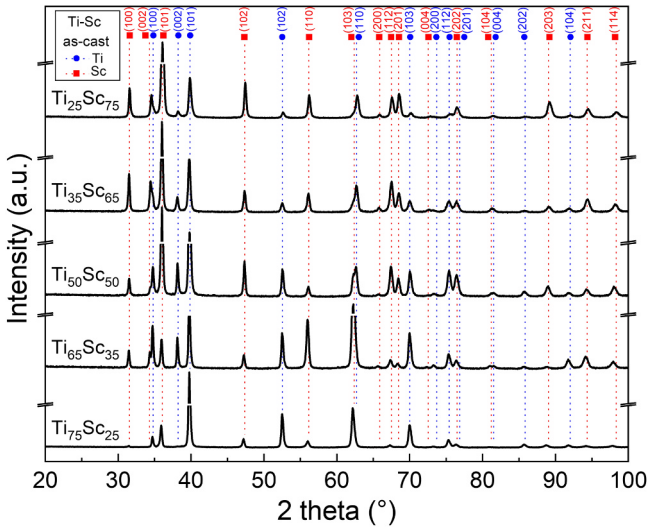


Fig. 1. X-ray diffractograms (CuKα) for bulk-cast samples of compositions (at %) from $Ti_{25}Sc_{75}$ to $Ti_{75}Sc_{25}$. The peaks are indexed separately for the Ti-rich and Sc-rich terminal solid solutions.

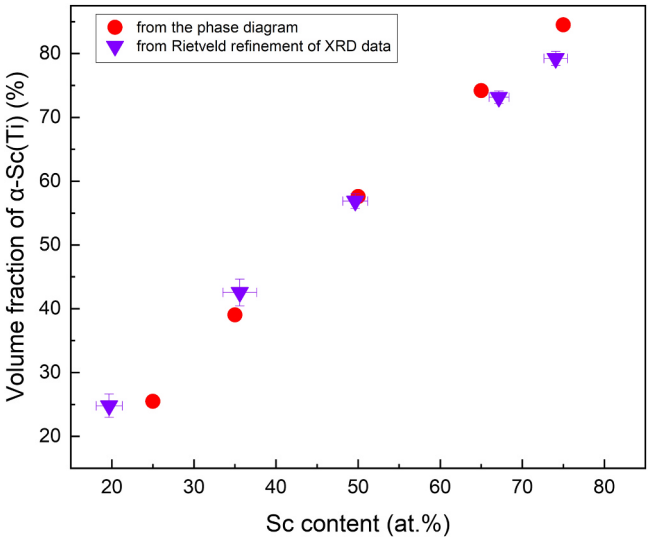


Fig. 2. The volume fraction of the α-Sc(Ti) terminal solid solution in bulk-cast alloys estimated, as a function of overall Sc content in the alloy, by applying the lever rule to the phase compositions (Table S3). The volume-fraction values are supported by semi-quantitative Rietveld analysis of the XRD data (Fig. 1 and Table S1); the estimated standard deviations in these Rietveld-derived values are shown as vertical error bars.

α-Sc); this approximation likely accounts for the discrepancies in values of volume fraction and overall sample composition (Fig. 2). Overall, the samples of different composition can be consistently interpreted as mixtures of different proportions of α-Ti(Sc) and α-Sc(Ti) that have the same well-defined compositions independent of overall sample composition.

3.2. Mechanism of microstructure formation

Scanning-electron micrographs of the as-cast two-phase solids are shown in Fig. S5. Immersion of these solids in a solution of 70% HNO_3 yields nanoporous Ti-rich samples, which have microstructures (Fig. 3) that correspond closely with the microstructures before immersion: the α-Sc(Ti) phase has selectively dissolved, while the α-Ti(Sc) phase appears unaffected. All the microstructures in Fig. 3 and Fig. S5 show clear alignment, characteristic of cooperative growth of two phases, of the kind familiar from eutectic and eutectoid transformations. In such cases, when the two phases are present in roughly equal proportions, a lamellar microstructure is expected. When one phase has a small volume fraction relative to the other, it appears as aligned parallel rods in a matrix of the other phase. For $Ti_{50}Sc_{50}$ and $Ti_{65}Sc_{35}$ (in which the two phases have similar volume fractions), the morphology revealed by the dissolution of α-Sc(Ti) is lamellar as expected. For $Ti_{75}Sc_{25}$, the Sc-rich phase (now etched away to leave voids) is in the form of rods of roughly circular cross-section and moderately uniformly spaced (Fig. 3f). In Fig. 3k, the rods are sliced at an angle such that the cross-section is elliptical. For $Ti_{25}Sc_{75}$, the rod-like nature of the Ti-rich phase is evident. For $Ti_{35}Sc_{65}$, the microstructure is a hybrid between lamellar and rod-like.

Just below the solidus on the Sc-Ti equilibrium diagram (Fig. S1), the body-centered cubic β-phase Sc-Ti solid solution spans the entire composition range. As already identified [14], this phase can exhibit spinodal decomposition, and it was suggested that this process could be responsible for the separation into the Ti-rich and Sc-rich phases found in as-cast Ti-Sc alloys. Spinodal decomposition is, however, not associated with aligned microstructures of the kind seen in Fig. 3. Roughly 20 K below the possible onset of spinodal decomposition (at around 37 at% Sc) on cooling β-(Sc-Ti), the solid solution undergoes a monotectoid decomposition with the appearance of a new phase: hexagonal close-packed (hcp) near-elemental α-Sc(Ti). This decomposition, and the subsequent widening of the (α+β) two-phase field upon cooling, are the origin of the division into two near-elemental solid solutions. From the alloy microstructures, we identify something not dictated by the equilibrium diagram: the mechanism of the appearance of α-Sc(Ti) must be cellular (discontinuous) precipitation.

The mechanism of cellular precipitation was comprehensively explored by Turnbull et al. [24–26] for the precipitation of tin from Pb-Sn solid solutions: cells nucleate on grain boundaries, and within these cells, the precipitating Sn-phase typically grows as lamellae interleaved with the Sn-depleted Pb-Sn matrix.

In the present case, within the β-(Sc-Ti) solid solution, cells are formed in which the new phase, hcp α-Sc(Ti), grows cooperatively with β-Ti(Sc) depleted in scandium. The β-Ti(Sc) phase subsequently transforms to hcp α-Ti(Sc), such that the final microstructure is essentially interleaved α-Sc and α-Ti. The phase compositions in bulk-cast samples (Fig. S3) are each consistent with a two-phase equilibrium in the range 910–935 °C just above the temperature of the β-Ti → α-Ti polymorphic transition. These compositions presumably indicate the lowest temperature at which compositional equilibrium in the phase field α-Sc(Ti) + β-Ti(Sc), could be maintained upon cooling.

3.3. Porosity and specific surface area

Samples subjected to selective dissolution (for 20 h), showed nanoporous surface layers extending (in the two cases examined) to a depth of ≥ 100 μm below the original surface (Fig. S6). This depth exceeds the penetration depth of the X-rays over the relevant Bragg-angle range, and the X-ray diffractograms show reflections exclusively from α-Ti(Sc) (Fig. S4), confirming the complete removal of the α-Sc(Ti) phase from the porous region.

The volume fraction of porosity can be estimated from SEM micrographs (Fig. 3f–j), with values in reasonable agreement with the volume fraction of α-Sc(Ti) in the corresponding bulk-cast alloys (Fig. 2). This consistency supports the interpretation that selective dissolution is effectively complete, with negligible dissolution of the Ti-rich phase and minimal structural collapse or distortion during the process. For the application of nanoporous samples, it is of course beneficial if they are mechanically robust. Handling of the samples in the present work showed this to be so, except for NP-Ti_{25}.

The specific surface area (SSA) of fully treated NP-Ti samples (immersed in acid for one week to ensure complete dissolution) was

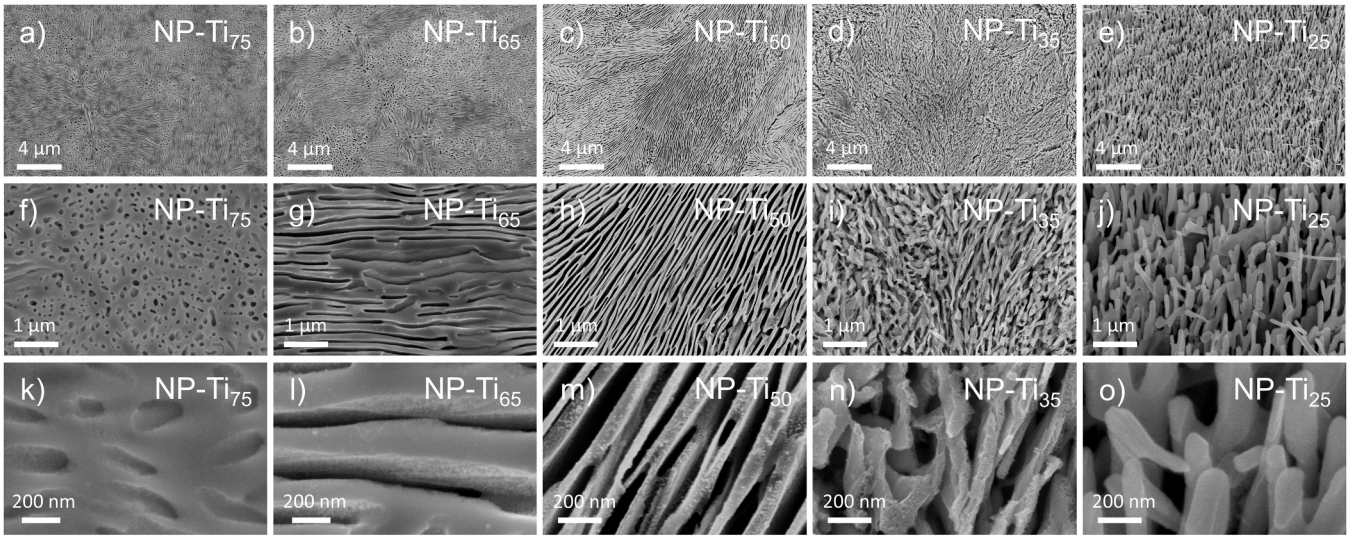


Fig. 3. SEM images of the nanoporous Ti produced by selective dissolution of the α-Sc(Ti) phase from the Ti-Sc alloys (Ti content given in at%). (a–e) low, (f–j) intermediate, and (k–o) high magnification.

determined using nitrogen adsorption and the BET method (Fig. S7). The measured SSA values (10–80 m^2 g^{-1}, Fig. 4a) span, and in some cases exceed, the typical range reported for nanoporous metals produced by conventional dealloying routes. Nanoporous Ag (5 m^2 g^{-1}) [7] and Au (3–10 m^2 g^{-1}) [27] have relatively low SSAs, consistent with the high atomic weights of these elements. Higher values are attained with lighter elements: Cu (10.8–12.3 m^2 g^{-1}) [28], Cu & Ti doped Cu (42 m^2 g^{-1}) [29], Nb (3.4–5.5 m^2 g^{-1}) [30,31], and α-Ti (34.4 m^2 g^{-1}) [32]. Foams of β-Ti15Mo made by spark plasma sintering reach SSA up to 29.0 m^2 g^{-1} [33].

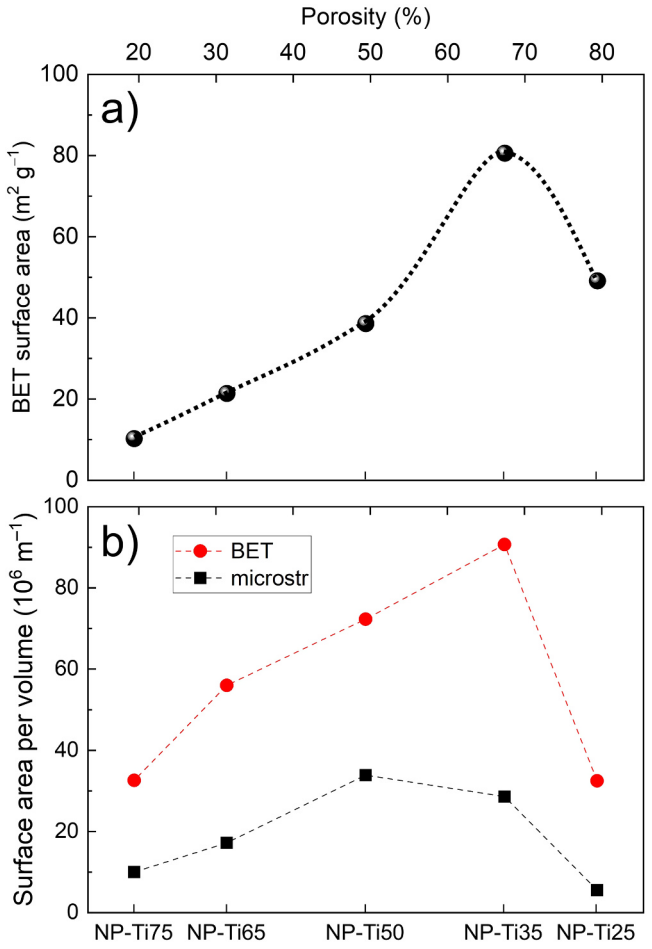


Fig. 4. Specific surface area (SSA) for the NP-Ti samples prepared from bulk-cast Ti-Sc alloys: (a) SSA per gram from BET measurements; (b) SSA per unit volume, from BET measurements and estimated from the microstructures of the samples.

Still higher SSA values can be attained when nanoporosity develops on a finer scale. The exceptionally high SSA of dealloyed Ti-V-Nb-Mo-Ta (55.7 m^2 g^{-1}) [34], for instance, is associated with ligaments of only 10 nm in diameter, roughly an order of magnitude finer than usual in dealloyed samples, a refinement attributed to slow microstructural coarsening in the high-entropy alloy.

The SSA can also be expressed per unit volume; values derived from BET measurements are compared in Fig. 4b with those estimated from the observed microstructures (Suppl. Mater. §S6, Table S5). While a clear correlation is observed, the BET-derived SSA values are systematically higher by a factor of 2–6.

This discrepancy likely arises from several factors. First, microstructure-based estimates are limited by resolution and may not capture nanoscale roughness or sub-ligament porosity, both of which contribute significantly to the accessible surface area. Secondly, the complex, tortuous morphology of the nanoporous network may include features such as necking, surface irregularities, or partially enclosed porosity that are not fully accounted for in simplified geometric models. Finally, the assumptions underlying the BET method—particularly the formation of uniform multilayer adsorption on idealized surfaces—may not be strictly valid for such heterogeneous metallic nanostructures.

Taken together, these considerations suggest that the true surface area lies between the geometric estimates and the BET-derived values, with the latter likely capturing additional contributions from fine-scale surface features. Despite these uncertainties, the consistent trends observed across compositions indicate that both approaches reliably reflect the influence of microstructural refinement on SSA.

3.4. *Wettability and contact angle*

Water droplets were released onto the surfaces of bulk-cast Ti-Sc samples, and of the NP-Ti samples obtained from them by selective dissolution, with the preliminary results shown in Fig. 5. For bulk-cast samples, the contact angle θ (approx. 75°) shows little, if any, variation with alloy composition, and indicates a mildly hydrophilic

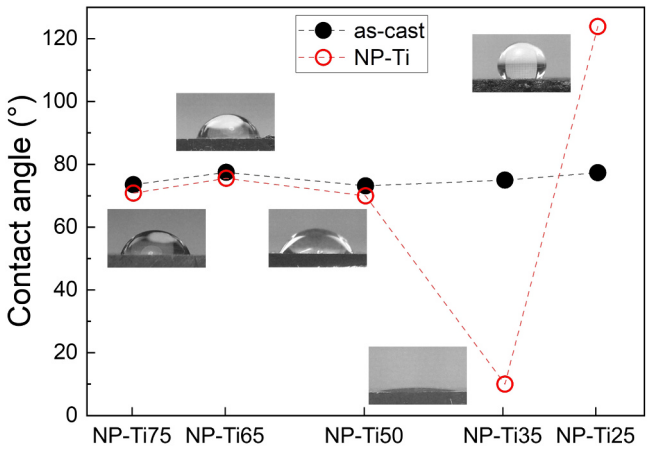


Fig. 5. The images show water droplets on NP-Ti prepared from the bulk-cast samples by selective dissolution. Droplets were also characterized on the corresponding as-cast Ti-Sc samples. Contact-angle values are compared for the as-cast samples (black solid circles) and the NP-Ti (red open circles).

interaction. For alloys with Sc contents up to and including 50 at%, the NP-Ti samples show virtually the same contact angle. This implies that for the porosities in these samples (at most 58%), the perimeter of the water spherical cap can trace a path on the alloy surface that is largely untroubled by the pores.

The NP-Ti_{35} sample shows a dramatically reduced contact angle of 10°. This accentuation of the hydrophilicity ($\theta < 90°$) on the smooth surface is characteristic of the Wenzel regime of wetting [35]. In this case, the water droplet was fully absorbed into the nanoporous solid within 5–10 s; in contrast, there were no visually detectable changes in the other NP-Ti samples during image acquisition (seconds-to-minutes timescale). In the Wenzel regime, the degree of roughness is characterized by the ratio R of the real over the projected surface area of the sample. The relationship between the contact angle θ on a smooth surface and the observed angle θ_{obs} on a rough surface is:

$$\cos\theta_{obs} = R\cos\theta \quad (1)$$

With $\theta = 75°$ and $\theta_{obs} = 10°$, we obtain $R \approx 3.8$, which can quantify the extent of water penetration into the porosity of the NP-Ti_{35} sample. If we assume penetration to a uniform depth, and take the SSA (m^{-1}) values from Fig. 4b, then $R = 3.8$ would correspond to a depth in the range from 39 nm (using SSA from BET) to 124 nm (using SSA from microstructure).

In contrast, the NP-Ti_{25} sample has a hydrophobic surface, with $\theta_{obs} \approx 124°$. This is characteristic of the Cassie-Baxter regime [36], in which the water droplet sits on top of the solid asperities, with the porosity filled with air. The relationship between contact angles is now:

$$\cos\theta_{obs} = f_s(1 + \cos\theta) - 1 \quad (2)$$

where f_s is the fraction of the projected surface area occupied by the solid. For a random section through a microstructure, f_s is simply the volume fraction of solid. For the $Ti_{25}Sc_{75}$ alloy, that is 0.155. Thus from Eq. (2) we predict $\theta_{obs} = 144°$, broadly consistent with the actual observed angle. This sample is close to superhydrophobicity ($\theta_{obs} \geq 150°$), and suggests that with some optimization that state might be attainable.

The change in wetting regime (hydrophilic–hydrophobic) is likely linked to the morphology of the solid ligaments. For NP-Ti_{25}, the rod-like (hairy) morphology favors the Cassie-Baxter regime. For NP-Ti_{35}, the hybrid morphology, in particular the residual lamellar nature, may favor the Wenzel regime.

3.5. Optical reflectivity

Both the total and diffuse reflectivities of the NP-Ti samples were measured. These were compared to those of polished and rough titanium, and matt-black paint. Fig. 6a–c show that the total reflectivity of polished titanium and as-cast Ti-Sc alloys is similar, and that the diffuse contribution to this is very low (below 5% on the normalized scale). Induced roughness on the titanium sample does not significantly change the total reflectivity but does drastically increase the diffuse scattering, to the extent that it becomes the dominant contribution to the total (Fig. 6d). For a flat surface covered with matt-black paint, the incident light is absorbed such that both total and diffuse reflectivity are minimal (Fig. 6e).

The NP-Ti samples all show low total and diffuse reflectivities, comparable to those of matt-black paint (Fig. 6f–j). The ratio of diffuse to total reflectivity is highest for matt-black paint. For decreased Ti content and therefore increased porosity, the (diffuse/total) reflectivity ratio of the NP-Ti samples is increased until, for NP-Ti_{35} and NP-Ti_{25}, it is essentially as high as that for the paint (Fig. 6k). Despite being metallic, the NP-Ti samples reflect and scatter incident light in such a way that they appear black (Fig. 6l).

3.6. Refinement of microstructure

As noted in §3.3, finer-scale microstructure leads to higher SSA. For the lamellar microstructures, the scale is characterized by the spacing λ (i.e. the perpendicular distance between the center-planes of neighboring lamellae of the same phase). This is taken to be the minimum observed spacing for each sample (values in Table S4). The value of λ depends on the cooling rate during the cellular precipitation. The effects of increased cooling rate are examined for $Ti_{50}Sc_{50}$ (at%), for which the precipitation occurs at least 250 K below the solidus temperature (Fig. S1). The possibility of achieving finer microstructure was demonstrated in earlier work [14]: λ was 51 nm in a bulk-cast sample, but as short as 23 nm when the sample was melt-spun. In melt-spinning the cooling rate is high (10^5–10^6 K s^{-1}) at the point of solidification, but is lower at the precipitation temperature. In the present work, a suction-cast rod of 2 mm diameter shows $\lambda \approx 22$ nm (Fig. 7), similar to the melt-spun sample. Such a halving of λ, compared to bulk-cast samples, should double the SSA.

We also explore whether solid-state quenching can reach cooling rates high enough to give usefully fine microstructures and high SSA. For bulk-cast $Ti_{50}Sc_{50}$ samples, Fig. 8 shows the effects of 4 h anneals followed by water-quenching. After annealing at 750 °C in the two-phase field α-Sc(Ti)–α-Ti(Sc), there is some coarsening (Fig. 8d–f); after annealing at 950 °C in the two-phase field α-Sc(Ti)–β-Ti(Sc), there is marked coarsening (Fig. 8g–i). In contrast, after annealing at 1150 °C in the single-phase field β-(Sc-Ti), there is microstructural refinement (Fig. 8j–l): the interlamellar spacing $\lambda = 59$ nm in the as-cast sample is reduced to 41 nm by annealing and quenching. This reduction in λ can be explained only if the annealing at 1150 °C is a solution-treatment that recovers the single-phase solid solution β-(Sc-Ti) that then undergoes renewed cellular precipitation upon subsequent quenching.

Annealing and water-quenching of suction-cast $Ti_{50}Sc_{50}$ gives similar effects (Fig. S9). The lamellar spacing λ after annealing at 1150 °C is again shorter than after 750 °C or 950 °C. In this case, however, it is not shorter than in the as-cast sample; the λ of 22 nm in the as-cast sample is increased to 130 nm by the annealing and quenching.

Interphase interfaces in the two-phase samples in the present work must impede plastic deformation. For higher interfacial area per unit volume (most easily quantified for lamellar microstructures through its inverse proportionality to λ), we expect (before any selective dissolution) samples of finer microstructure to have higher hardness. As explored in Section S8, hardness measurements are convenient in monitoring the effects of heat treatments on microstructure (and therefore on SSA and related properties of the NP-Ti obtained by

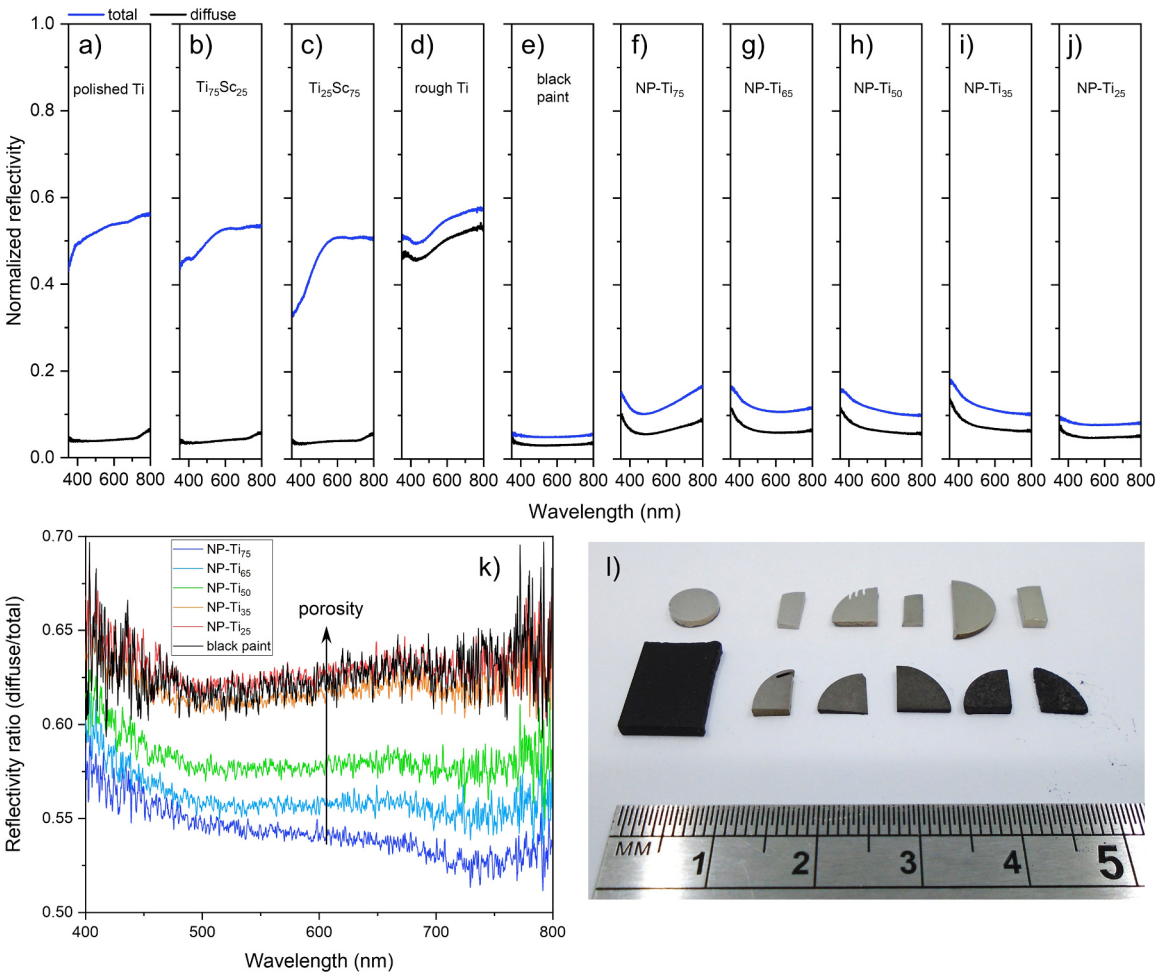


Fig. 6. Normalized total and diffuse reflectivities of: (a) polished bulk Ti; (b,c) bulk-cast Ti-rich and Sc-rich Ti-Sc alloys in the present work; (d) mechanically roughened bulk Ti; (e) matt-black paint; and (f–j) the NP-Ti alloys in the present work. Data over the full spectral range are given in Fig. S8. (k) Ratio of the diffuse to total reflectivity of NP-Ti samples compared to that of matt-black paint. (l) Photographs: top row: Ti (left) and bulk-cast Ti-Sc alloys (Sc at% increasing from left to right); bottom row: matt-black painted sample (left) and NP-Ti samples (porosity increasing from left to right).

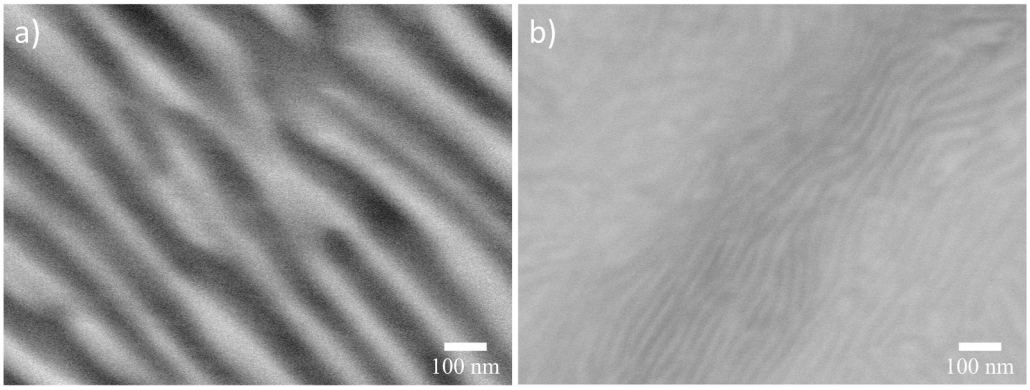


Fig. 7. Comparison of (a) bulk-cast and (b) suction-cast $Ti_{50}Sc_{50}$ showing the finer lamellar microstructure in the latter case. The bulk-cast sample is more deeply etched than the suction-cast rod.

selective dissolution).

The microstructural scale, and therefore SSA, of nanoporous samples obtained by selective dissolution can, usefully, be influenced by both casting conditions and subsequent heat treatment. Of all the $Ti_{50}Sc_{50}$ samples studied, the suction-cast 2-mm-diameter rod has the finest lamellar microstructure ($\lambda = 22$ nm). However, bulk-cast samples can reach broadly similar λ by annealing at 1150 °C and water-quenching. The possibilities of solid-state thermal processing to achieve yet finer microstructure and higher SSA remain to be explored.

3.7. Discussion

The present results show that cellular precipitation in the solid state is a route to fine two-phase microstructures that by selective dissolution

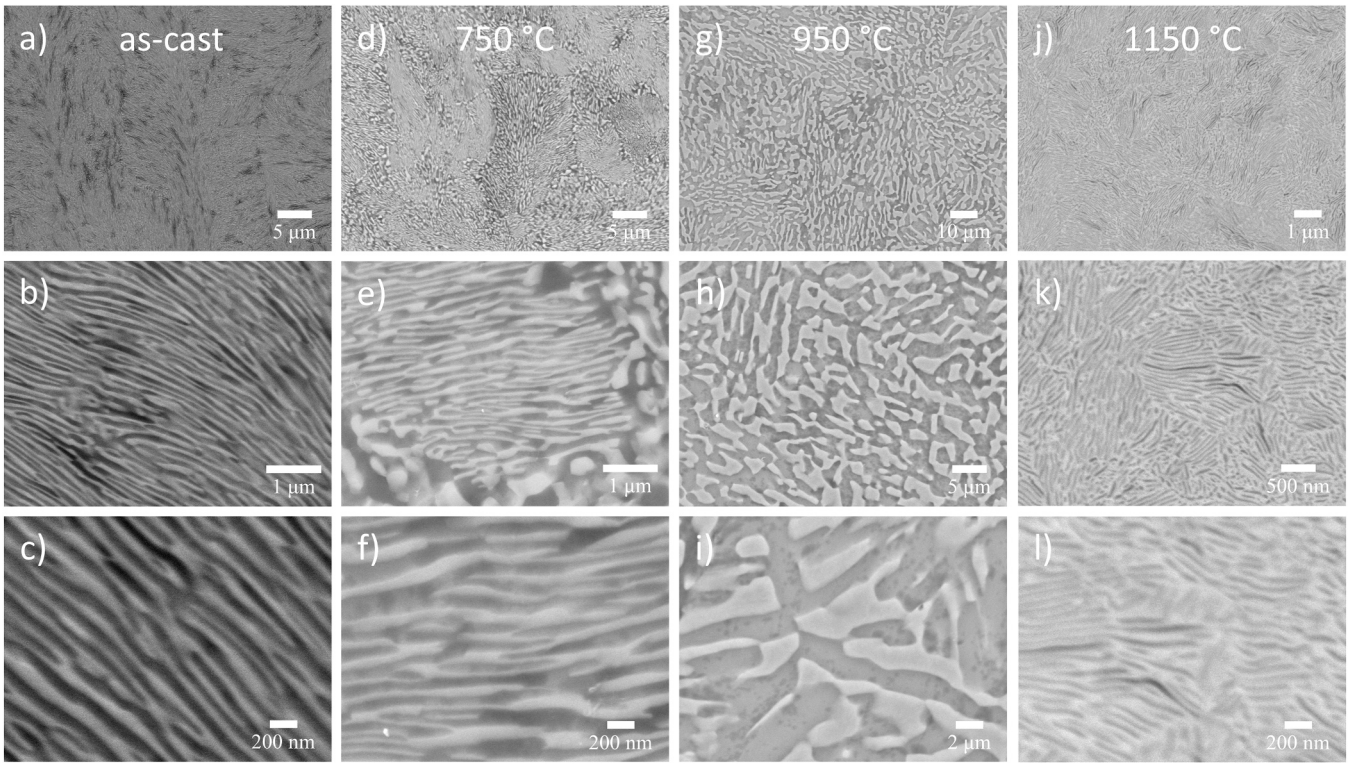


Fig. 8. SEM micrographs of surface-etched bulk $Ti_{50}Sc_{50}$ (at%) alloys: (a–c) as-cast, and annealed for 4 h at: (d–f) 750 °C; (g–i) 950 °C; (j–l) 1150 °C.

of one of the phases can yield nanoporous metals. The specific surface areas thus obtained compare favorably with those obtained by the usual dealloying routes. By varying the volume fractions of the two phases, some control of the microstructure (lamellar or rod-like) is possible.

Scandium is an expensive element. The extent to which this would impede applications has been briefly discussed [15]. In any case, for selective dissolution from Ti-Sc alloys to be a practicable route to NP-Ti samples, efficient recovery of the scandium from the acid mixture would be necessary. The Ti-Sc system can be considered as a 'proof of concept' for a cellular-precipitation route to nanoporous solids. Cellular precipitation has been studied in Pb-Sn [24–26], Ag-Cu, Cu-Ag and Cu-Cd [37], Cu-In [38] and Zn-Ag [39], and may occur in many other cases. At least, it can be added to eutectoid decomposition as a solid-state transformation that can yield fine-scale two phase microstructures that may be useful for the production of nanoporous metals by selective phase dissolution. Thereby, it must widen the range of alloy compositions that can be obtained in nanoporous form. As noted in §1, the separation of microstructural development and dissolution can increase the degree of control over that achievable in dealloying. That control may be exercised through both the casting conditions and subsequent solid-state heat treatment.

For the particular case of nanoporous titanium, the combination of high specific surface area, tunable wettability, and low optical reflectivity may be attractive for several functional applications. Possible areas of interest include: light-management surfaces, photothermal systems, catalytic supports, and biomedical implants, where the open porous architecture and chemical stability of titanium may be advantageous. In addition, the black appearance arising from strong light scattering rather than pigment absorption may be relevant for optical and thermal-management applications. These aspects warrant further investigation.

4. Conclusions

A series of alloys from $Ti_{75}Sc_{25}$ to $Ti_{25}Sc_{75}$ (at%) has been studied. The as-cast alloys consist of two near-elemental phases; α-Ti(Sc) and α-Sc(Ti). The phase morphologies vary systematically with composition: lamellar in the middle of the composition range and rod-like at the extremes. The key mechanism of the microstructural development is identified as cellular precipitation. By selective dissolution in acid, the α-Sc(Ti) phase can be completely removed, yielding nanoporous titanium (NP-Ti) samples. The specific surface area (SSA) of these samples, measured by the BET method, is in the range 10–80 $m^2\ g^{-1}$, competitive with values attainable by dealloying methods. These SSA values are 2–6 times those directly expected from the observed microstructures. NP-Ti_{25} is strongly hydrophobic; the next most porous sample, NP-Ti_{35}, is strongly hydrophilic. This contrast in wettability can be understood from the microstructures and standard wetting models (Wenzel and Cassie-Baxter). The most porous samples, despite being entirely metallic, are matt-black. Cellular precipitation, followed by selective dissolution of one phase, is a useful addition to the range of techniques for producing nanoporous metals. There is much scope for process optimization (in solidification and subsequent heat-treatment) to control the morphology of the porosity and to increase the SSA.

CRediT authorship contribution statement

N.T. Panagiotopoulos: Writing – original draft, Visualization, Validation, Methodology, Investigation, Formal analysis, Data curation, Conceptualization. **A.L. Greer:** Writing – review & editing, Visualization, Validation, Methodology, Funding acquisition, Formal analysis, Conceptualization. **A.M. Jorge:** Writing – review & editing, Validation, Resources, Investigation, Funding acquisition, Formal analysis. **L. Koutsokeras:** Writing – original draft, Visualization, Validation, Investigation, Formal analysis, Data curation. **G.I. Lampronti:** Writing – review & editing, Formal analysis, Data curation. **W.J. Botta:** Writing – review & editing, Validation, Resources. **K. Georgarakis:** Writing – review & editing, Validation, Resources, Methodology.

Declaration of Competing Interest

The authors declare the following financial interests/personal relationships which may be considered as potential competing interests: A. L. Greer reports financial support was provided by European Research Council. N. T. Panagiotopoulos reports financial support was provided by European Research Council. A. M. Jorge Jr reports financial support was provided by State of Sao Paulo Research Foundation. A. M. Jorge Jr reports financial support was provided by National Council for Scientific and Technological Development. If there are other authors, they declare that they have no known competing financial interests or personal relationships that could have appeared to influence the work reported in this paper.

Acknowledgements

This work is dedicated to the memory of the late Prof. A.R. Yavari, whose vision initiated this study. NTP and ALG acknowledge support from the European Research Council under the European Union's Horizon 2020 research and innovation program (grant ERC−2015-AdG-695487: Extend Glass). AMJ acknowledges support from the São Paulo Research Foundation - FAPESP (Brazil) under grant FAPESP #2021/06546–1 and the National Council for Scientific and Technological Development – CNPq (Brazil) under grant CNPq# 306622/2021–1. The authors are also grateful to the Laboratory of Structural Characterization of the Federal University of São Carlos (LCE/Dema/UFSCar-Brazil) and Le Consortium des Moyens Technologiques Communs (CMTC – Grenoble-INP-France) for the use of their facilities.

Appendix A. Supporting information

Supplementary data associated with this article can be found in the online version at doi:10.1016/j.jallcom.2026.189327.

References

[1] L. Tian, A. Soum-Glaude, F. Volpi, L. Salvo, G. Berthomé, S. Coindeau, A. Mantoux, R. Boichot, S. Lay, V. Brizé, E. Blanquet, G. Giusti, D. Bellet, Undoped TiO_2 and nitrogen-doped TiO_2 thin films deposited by atomic layer deposition on planar and architectured surfaces for photovoltaic applications, J. Vac. Sci. Technol. A 33 (2015) 01A141, https://doi.org/10.1116/1.4904025.

[2] R. Ramesh, S. Niauzorau, V.K. Sampath, L. Wang, B.P. Azeredo, situ temperature dependent optical characterization and modeling of dealloyed thin-film nanoporous gold absorbers, Adv. Opt. Mater. 10 (2022) 2102479, https://doi.org/10.1002/adom.202102479.

[3] J. Fu, Z. Li, X. Li, F. Sun, L. Li, H. Li, J. Zhao, J. Ma, Hierarchical porous metallic glass with strong broadband absorption and photothermal conversion performance for solar steam generation, Nano Energy 106 (2023) 108019, https://doi.org/10.1016/j.nanoen.2022.108019.

[4] L.H. Qian, X.Q. Yan, T. Fujita, A. Inoue, M.W. Chen, Surface enhanced Raman scattering of nanoporous gold: Smaller pore sizes stronger enhancements, Appl. Phys. Lett. 90 (2007) 153120, https://doi.org/10.1063/1.2722199.

[5] A.N. Koya, X. Zhu, N. Ohannesian, A.A. Yanik, A. Alabastri, R. Proietti Zaccaria, R. Krahne, W.-C. Shih, D. Garoli, Nanoporous metals: From plasmonic properties to applications in enhanced spectroscopy and photocatalysis, ACS Nano 15 (2021) 6038–6060, https://doi.org/10.1021/acsnano.0c10945.

[6] J. Zhang, C.M. Li, Nanoporous metals: Fabrication strategies and advanced electrochemical applications in catalysis, sensing and energy systems, Chem. Soc. Rev. 41 (2012) 7016–7031, https://doi.org/10.1039/c2cs35210a.

[7] D. Barsuk, A. Zadick, M. Chatenet, K. Georgarakis, N.T. Panagiotopoulos, Y. Champion, A.M. Jorge, Jr, Nanoporous silver for electrocatalysis application in alkaline fuel cells, Mater. Des. 111 (2016) 528–536, https://doi.org/10.1016/j.matdes.2016.09.037.

[8] Y. Shi, W. Yang, Q. Bai, J. Qin, Z. Zhang, Alloying/dealloying mechanisms, microstructural modulation and mechanical properties of nanoporous silver via a liquid metal-assisted alloying/dealloying strategy, J. Alloy. Compd. 872 (2021) 159675, https://doi.org/10.1016/j.jallcom.2021.159675.

[9] H. Zhao, D. Lei, Y.-B. He, Y. Yuan, Q. Yun, B. Ni, W. Lv, B. Li, Q.-H. Yang, F. Kang, J. Lu, Compact 3D copper with uniform porous structure derived by electrochemical dealloying as dendrite-free lithium metal anode current collector, Adv. Energy Mater. 8 (2018) 1800266, https://doi.org/10.1002/aenm.201800266.

[10] J. Erlebacher, M.J. Aziz, A. Karma, N. Dimitrov, K. Sieradzki, Evolution of nanoporosity in dealloying, Nature 410 (2001) 450–453, https://doi.org/10.1038/35068529.

[11] I. McCue, A. Karma, J. Erlebacher, Pattern formation during electrochemical and liquid metal dealloying, MRS Bull. 43 (2018) 27–34, https://doi.org/10.1557/mrs.2017.301.

[12] G. Scandura, P. Kumari, G. Palmisano, G.N. Karanikolos, J. Orwa, L.F. Dumée, Nanoporous dealloyed metal materials processing and applications – A Review, Ind. Eng. Chem. Res. 62 (2023) 1736–1763, https://doi.org/10.1021/acs.iecr.2c03952.

[13] J. Ying, S. Lenaerts, M.D. Symes, X.-Y. Yang, Hierarchical design in nanoporous metals, Adv. Sci. 9 (2022) 2106117, https://doi.org/10.1002/advs.202106117.

[14] N.T. Panagiotopoulos, A. Moreira Jorge, I. Rebai, K. Georgarakis, W.J. Botta, A. R. Yavari, Nanoporous titanium obtained from a spinodally decomposed Ti alloy, Micro Mesopor. Mater. 222 (2016) 23–26, https://doi.org/10.1016/j.micromeso.2015.09.054.

[15] A.M. Russell, Y. Tian, J.D. Rose, T.W. Ellis, L.S. Chumbley, A high specific strength, deformation-processed scandium-titanium composite, J. Mater. Res. 14 (1999) 8–11, https://doi.org/10.1557/JMR.1999.0003.

[16] K. Tiwari, D. Raj, P. Rizzi, F. Scaglione, Advances in dealloying of Ti and Ti-based alloys for biomedical applications, Materials 18 (2025) 4424, https://doi.org/10.3390/ma18184424.

[17] E. Vassileva, L. Mihaylov, T. Boyadjieva, V. Koleva, R. Stoyanova, T. Spassov, Porous Sn obtained by selective electrochemical dissolution of melt-spun $Zn_{70}Sn_{30}$ alloys with lithium and sodium storage properties, J. Alloy. Compd. 877 (2021) 160319, https://doi.org/10.1016/j.jallcom.2021.160319.

[18] E. Vassileva, L. Mihaylov, M. Spassova, T. Spassov, Porous metallic structures by de-alloying microcrystalline melt-spun ternary $Zn_{70}(Sn,Bi)_{30}$, J. Porous Mater. 30 (2023) 485–492, https://doi.org/10.1007/s10934-022-01361-8.

[19] R.I. Tomov, L. Mihaylov, L.R. Bird, E. Vassileva, R.V. Kumar, M. Chhowalla, T. Spassov, On the performance of a hierarchically porous Ag_2S-Cu_xS electrode in Li-ion batteries, Dalt. Trans. 51 (2022) 18045–18053, https://doi.org/10.1039/d2dt02880h.

[20] A.A. Coelho, TOPAS, TOPAS-Academic: An optimization program integrating computer algebra and crystallographic objects written in C++, J. Appl. Crystallogr. 51 (2018) 210–218, https://doi.org/10.1107/S1600576718000183.

[21] I.C. Madsen, N.V.Y. Scarlett, in: R.E. Dinnebier, S.J.L. Billinge (Eds.), Powder Diffraction: Theory and Practice, The Royal Society of Chemistry, 2008, pp. 298–331, https://doi.org/10.1039/9781847558237-00298, ch. 11.

[22] C.A. Schneider, W.S. Rasband, K.W. Eliceiri, NIH Image to ImageJ: 25 years of image analysis, Nat. Methods 9 (2012) 671–675, https://doi.org/10.1038/nmeth.2089.

[23] Sc (Scandium) Binary Alloy Phase Diagrams, in: H. Okamoto, M.E. Schlesinger, E. M. Mueller (Eds.), Alloy Phase Diagrams, ASM Handbook, Vol 3, ASM International, 2016, pp. 590–591, https://doi.org/10.31399/asm.hb.v03.a0006203.

[24] K.N. Tu, D. Turnbull, Morphology of cellular precipitation of tin from lead-tin bicrystals, Acta Metall. 15 (1967) 369–376, https://doi.org/10.1016/0001-6160(67)90214-3.

[25] K.N. Tu, D. Turnbull, Morphology of cellular precipitation of tin from lead-tin bicrystals-II, Acta Metall. 15 (1967) 1317–1323, https://doi.org/10.1016/0001-6160(67)90007-7.

[26] D. Turnbull, Theory of cellular precipitation, Acta Metall. 3 (1955) 55–63, https://doi.org/10.1016/0001-6160 (55)90012-2.

[27] M.M. Collinson, Nanoporous gold electrodes and their applications in analytical chemistry, ISRN Anal. Chem. 2013 (2013) 692484, https://doi.org/10.1155/2013/692484.

[28] X. Luo, R. Li, Z. Liu, L. Huang, M. Shi, T. Xu, T. Zhang, Three-dimensional nanoporous copper with high surface area by dealloying Mg-Cu-Y metallic glasses, Mater. Lett. 76 (2012) 96–99, https://doi.org/10.1016/j.matlet.2012.02.028.

[29] J.D. Lee, Z. Qi, A.C. Foucher, H.T. Ngan, K. Dennis, J. Cui, I.I. Sadykov, E. J. Crumlin, P. Sautet, E.A. Stach, C.M. Friend, R.J. Madix, J. Biener, Facilitating hydrogen dissociation over dilute nanoporous Ti-Cu catalysts, J. Am. Chem. Soc. 144 (2022) 16778–16791, https://doi.org/10.1021/jacs.2c00830.

[30] J.W. Kim, M. Tsuda, T. Wada, K. Yubuta, S.G. Kim, H. Kato, Optimizing niobium dealloying with metallic melt to fabricate porous structure for electrolytic capacitors, Acta Mater. 84 (2015) 497–505, https://doi.org/10.1016/j.actamat.2014.11.002.

[31] J.W. Kim, T. Wada, S.G. Kim, H. Kato, Enlarging the surface area of an electrolytic capacitor of porous niobium by Mg-Ce eutectic liquid dealloying, Scr. Mater. 122 (2016) 68–71, https://doi.org/10.1016/j.scriptamat.2016.05.014.

[32] F. Zhang, P. Li, J. Yu, L. Wang, F. Saba, G. Dai, S. He, Fabrication, formation mechanism and properties of three-dimensional nanoporous titanium dealloyed in metallic powders, J. Mater. Res. 32 (2017) 1528–1540, https://doi.org/10.1557/jmr.2017.19.

[33] F. Zhang, L. Wang, P. Li, S. Liu, P. Zhao, G. Dai, S. He, Preparation of nano to submicro-porous TiMo foams by spark plasma sintering, Adv. Eng. Mater. 19 (2017) 1600600, https://doi.org/10.1002/adem.201600600.

[34] S.-H. Joo, J.W. Bae, W.-Y Park, Y. Shimada, T. Wada, H.S. Kim, A. Takeuchi, T. J. Konno, H. Kato, I.V. Okulov, Beating thermal coarsening in nanoporous materials via high-entropy design, Adv. Mater. 32 (2020) 1906160, https://doi.org/10.1002/adma.201906160.

[35] R.N. Wenzel, Resistance of solid surfaces to wetting by water, Ind. Eng. Chem. 28 (1936) 988–994, https://doi.org/10.1021/ie50320a024.

[36] A.B.D. Cassie, S. Baxter, Wettability of porous surfaces, Trans. Faraday Soc. 40 (1944) 546–551, https://doi.org/10.1039/tf9444000546.

[37] M.S. Sulonen, Discontinuous mode of dissolution of a β phase precipitate into α Cu-Cd solid solutions, Acta Metall. 8 (1960) 669–676, https://doi.org/10.1016/0001-6160(60)90197-8.
[38] I. Manna, S.K. Pabi, W. Gust, Discontinuous precipitation in a Cu-12 at% In alloy, Acta Metall. Mater. 39 (1991) 1489–1496, https://doi.org/10.1016/0956-7151(91)90234-R.
[39] W. Xu, Y.P. Feng, Y. Li, Initiation of discontinuous precipitation at interphase boundaries in a two-phase Zn–6.3 at% Ag alloy, Philos. Mag. 84 (2004) 1773–1787, https://doi.org/10.1080/14786430310001639888.



https://dspace.org/

Selective phase dissolution as a route to nanoporous titanium with tailored properties

Panagiotopoulos, Nikolaos T.; Koutsokeras, Loukas E.; Jorge Junior, Alberto; Lampronti, Giulio I.; Georgarakis, Konstantinos ...

2026-07-10
Elsevier
https://doi.org/10.1016/j.jallcom.2026.189327
Panagiotopoulos NT, Koutsokeras L, Jorge AM, et al., (2026) Selective phase dissolution as a route to nanoporous titanium with tailored properties. Journal of Alloys and Compounds, Volume 1076, July 2026, Article number 189327

Downloaded from a DSpace repository. https://dspace.org/